nature communications

Article

https://doi.org/10.1038/s41467-025-67290-7

Rational electrolyte solvent screening for high-energy lithium metal batteries at low temperatures

Received: 15 May 2025

Accepted: 26 November 2025

Zehang Peng[1,4], Kui Ding[1,4], Meiting Lai[1], Rui Qiu[1], Ye Xiao[1], Junkai Shi[1], Xiaoxian Guan[1], Yue-Peng Cai[1], Chao Xu[2], Fei Wang[3] & Qifeng Zheng[1] ✉

Weakening the solvation ability has shown great potential in electrolyte solvent design to promote the cycling performance of Li-metal batteries, yet suffers from sluggish kinetics and uncontrolled Li dendrite formation, particularly at low temperatures. Herein, we propose a guideline for rational electrolyte solvent screening, where the restrained electrostatic potential of the coordinated O is proposed as one descriptor to quantify the solvation effect, followed by introducing the dipole moment as a correction descriptor to optimize solvents' sensitivity to the electric fields and interphase stability. Under the guidance of this screening principle, a class of asymmetric fluorinated ethers is rationally designed, of which the 3,3,3-trifluoropropyl-1-methyl ether with moderate restrained electrostatic potential of the coordinated O and dipole moment is identified to mediate a stable six-membered chelating structure with Li^+, significantly promoting Li kinetics and reversibility from 30 to −60 °C. Coupled with its good anodic stability, this single-salt single-solvent electrolyte enables the 50 μm Li||4.0 mAh cm^{-2} $LiNi_{0.8}Mn_{0.1}Co_{0.1}O_2$ coin-cells maintaining > 90% capacity after 200 cycles at benign and low temperatures. A practical Li-metal pouch-cell delivers a high specific energy (based on the mass of all components) of 345.3 Wh kg^{-1} over 40 cycles at −40 °C.

Li-metal batteries (LMBs) hold great promise to push the battery specific energy over 400 Wh kg^{-1} due to the high theoretical capacity (3860 mAh g^{-1}), low density (0.534 g cm^{-3}), and the lowest reduction potential (−3.04 V vs standard hydrogen electrode, SHE) of Li-metal negative electrodes[1–4]. Nevertheless, the high reactivity of Li-metal coupled with large volume change during charging/discharging inevitably induces the formation of unstable solid electrolyte interphase (SEI) and uneven deposition of Li, leading to the growth of Li dendrites and formation of dead Li[4,5], which yields low Coulombic efficiency (CE) and largely restricts the cycling life of LMBs. These issues will be further exacerbated when operating the LMBs at low temperatures (<−30 °C) owing to the sluggish kinetics[6,7], which howbeit is eagerly needed for subsea operations, polar expedition, and border patrol applications.

Electrolyte engineering offers a cost-effective and efficient approach to mitigate the above issues[8]. To fulfill the demand for high-energy and low-temperature LMBs, the following critical requirements for electrolytes should be met simultaneously, (i) the ability to form robust and conductive SEI to enable rapid Li^+ migration and highly reversible Li plating/stripping; (ii) fast Li^+ de-solvation kinetics while maintaining sufficient Li salt dissociation; (iii) high anodic stability to match the high-voltage and high-capacity layered positive electrodes such as Ni-rich $LiNi_{0.8}Mn_{0.1}Co_{0.1}O_2$ (NMC811). Numerous electrolyte design strategies have been proposed, including functional

---

[1]School of Chemistry, Guangzhou Key Laboratory of Materials for Energy Conversion and Storage, South China Normal University, Guangzhou, Guangdong, China. [2]MOE Key Laboratory of Environmental Theoretical Chemistry, South China Normal University, Guangzhou, Guangdong, China. [3]Department of Materials Science, Shanghai Key Laboratory of Molecular Catalysis and Innovative Materials, Fudan University, Shanghai, China. [4]These authors contributed equally: Zehang Peng, Kui Ding. ✉e-mail: Qifeng.Zheng@m.scnu.edu.cn

additives[9,10], high concentration electrolytes (HCEs)[11–15], localized high-concentration electrolytes (LHCEs)[16–18], and weakly solvated electrolytes (WSEs)[19–24].

Among the various electrolyte design strategies, weakening the solvation ability of the solvent through steric hindrance, changing chelation sites or structures, and incorporating fluorination represent the most promising approach. The reduced Li^+–solvent coordination will not only promote the de-solvation process but also intensify the Li^+–anion pairing to facilitate the formation of anion-derived inorganic-rich SEI at a regular concentration, which enhances the electrochemical kinetics and reversibility simultaneously. The well-explored 1,2-dimethoxyethane (DME) solvent featuring ethylene glycol backbone (i.e., bidentate) tends to chelate with Li^+ in a stable five-membered ring configuration, yet suffers from high de-solvation energy. By substituting the methoxy groups on DME with larger-sized ethoxy groups, Chen et al. reported a 1,2-diethoxyethane (DEOE) electrolyte with weakened Li^+ solvation and enhanced Li CE[15]. Li et al. further methylated the inner α-H of DEOE to form 1,2-diethoxypropane (DEP), which further reduces its solvation power and thus improving the Li CE to ~99.5%[23]. In addition, Yu et al. rationally tuned the ethoxy group of DEOE with partially or fully fluorinated moieties, which yields high Li CEs of > 99.5% and enables the stable operation of high-voltage NMC811 cells[20]. Recently, Choi et al. proposed the asymmetric molecular design strategy to ether with only one side being fluorinated, the resulting asymmetric 1-(2,2,2-trifluoro)-ethoxy-2-methoxyethane (F3EME) bestows fast redox kinetics for high-power LMBs[23].

Alternative to the well-explored DME series solvent with bidentate sites, the monodentate ether possesses much lower solvation power that offers great potential for operating the LMBs at low temperatures. Holoubek et al. employed diethyl ether (DEE) to tailor the electrolyte solvation structure, which enables the Li||sulfurized polyacrylonitrile (SPAN) coin cells to retain 84% and 76% of its room temperature capacity when cycled at −40 and −60 °C, respectively[7]. Zhang et al. chose a binary solvent consisting of DEE and DME solvents (DEE: DME = 9:1 vol%) with the aid of 0.1 M perfluoroalkylsulfonyl quaternary ammonium nitrate (PQA-NO_3), the developed electrolyte demonstrated stable cycling of Li||NMC811 coin cell at −60 °C[10]. Wei et al. reported a 2,2-difluoroethyl acetate (EA-2F) solvent with local dipole to enable the operation of Li||$LiNi_{0.6}Mn_{0.2}Co_{0.2}O_2$ (NMC622) pouch cell with a high specific energy of 350 Wh kg^{-1} for 75 cycles at −20 °C[25]. Despite the encouraging progress has been made, achieving stable cycling of LMBs with practically high specific energy beyond 300 Wh kg^{-1} under low temperatures (<−30 °C) is unattainable for the current reported electrolytes. Moreover, excessively weakening the solvation ability will result in low ionic conductivity, thereby hindering the Li^+ transport in bulk electrolyte. Therefore, the structure of the solvent must be regulated carefully to balance the kinetics of ion transport, de-solvation, and Li^+ migration through SEI.

In this work, we design a series of asymmetric ether solvents (Fig. 1a) and quantify their solvation ability. As shown in Fig. 1b, the appropriate ion-dipole interactions were established by introducing dual descriptors of the restrained electrostatic potential (RESP)[26–29] of the coordinated O (denoted as $RESP_O$) and dipole moment (μ), facilitating rational solvent screening for LMBs electrolytes. Applying this $RESP_O$–μ selection principle, we identify 3,3,3-trifluoropropyl-1-methyl ether (TFPM) as a promising solvent to enable high-energy LMBs at low temperatures. The TFPM-based electrolyte induces a stable six-membered chelating solvation structure through Li-F and Li-O bi-coordination (Fig. 1c), which is expected to enhance the ionic conductivity, de-solvation kinetics, and interfacial stability simultaneously, thus enabling highly reversible Li plating/stripping and uniform deposition morphologies from 30 to −60 °C. Furthermore, 50 μm Li||4.0 mAh cm^{-2} NMC811 practical cells using TFPM electrolyte demonstrate > 200 cycles at both 30 °C and −40 °C. Notably, a prototype Li||$LiNi_{0.9}Mn_{0.05}Co_{0.05}O_2$ (NMC9055) pouch cell demonstrates a high specific energy of 345.3 Wh kg^{-1} at −40 °C and can stably operate for 40 cycles with 90.8% capacity retention.

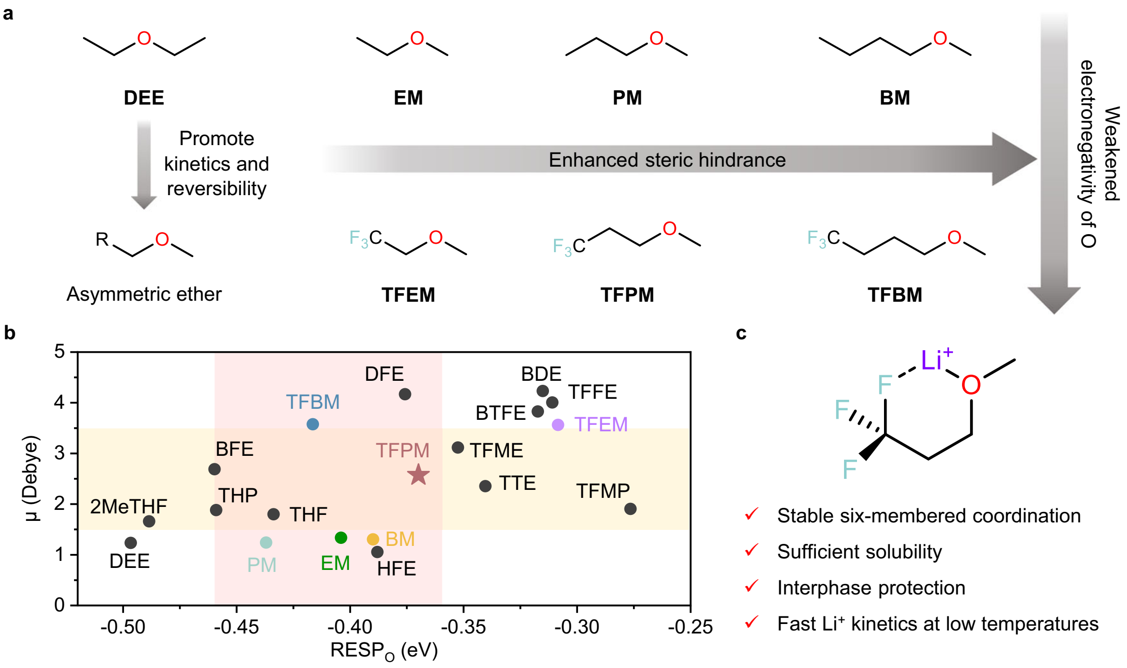

Fig. 1 | Design rationale and selection principle of solvents. a Design rationale of asymmetric ethers derived from monodentate DEE. **b** Selection principle based on dual descriptors of $RESP_O$ and μ. **c** Illustration of six-membered chelating structure of TFPM with Li^+. DEE diethyl ether, THF tetrahydrofuran, 2MeTHF 2-methyltetrahydrofuran, THP tetrahydropyran, BTFE bis(2,2,2-trifluoroethyl) ether, BDE bis(2,2-difluoroethyl) ether, TFFE 2,2,2-trifluoroethyl-2-fluoroethyl ether, DFE 2,2-difluoroethyl-2-fluoroethyl ether, BFE bis(2-fluoroethyl) ether, TFME 1,1,2,2-tetrafluoroethyl methyl ether, TFMP 1,1,2,2-tetrafluoro-3-methoxypropane, TTE 1,1,2,2-tetrafluoroethyl-2,2,3,3-tetrafluoropropyl ether, HFE 1,1,2,2-tetrafluoroethyl-2,2,2-trifluoroethyl ether. Source data are provided as a Source Data file.

Results

Solvent design rationale and screening principle

Ether solvents demonstrate good stability towards Li-metal, of which their solvation ability plays a critical role in governing Li^+–anion interactions, solubility, ionic conductivity, and viscosity. The solvent with weak solvation ability could enhance Li^+–anion coordination to promote anion-derived inorganic-rich SEI, while it often compromises the solubility and ionic conductivity. The monodentate DEE solvent demonstrates weak solvation ability with good Li-metal compatibility at low temperatures, yet suffers from poor rate capability and anodic stability[7,30]. Based on our prior study[31] as well as recent publications[32,33] that validates the efficacy of asymmetric ether design strategy in improving Li redox reversibility and kinetics, we initiate the asymmetric design to the monodentate ether solvent by retaining methoxy groups to ensure adequate Li^+ coordination while leveraging alkyl groups with different steric hindrance to regulate solvation ability, yielding a series of asymmetric ethers, namely, ethyl methyl ether (EM), n-propyl methyl ether (PM), and n-butyl methyl ether (BM). To enhance the oxidation stability and promote the inorganic SEI, fluorination was further introduced to generate a series of asymmetric fluorinated ethers, including 2,2,2-trifluoroethyl methyl ether (TFEM), 3,3,3-trifluoropropyl methyl ether (TFPM), and 4,4,4-trifluorobutyl methyl ether (TFBM). Notably, none of the asymmetric fluorinated ethers designed herein are commercially available. A two-step reaction has been successfully used for the synthesis of all fluorinated ethers (Supplementary Fig. 1). The structures were confirmed by nuclear magnetic resonance (NMR) spectra, including ^1H NMR, ^{13}C NMR, and ^{19}F NMR (Supplementary Figs. 2–4). The general physicochemical properties of all solvents are shown in the Supplementary Table 1. Due to impractical low boiling point of EM (~7 °C) and poor solubility of TFEM [< 0.1 M for lithium bis(fluorosulfonyl)imide (LiFSI)], they were excluded from further analysis with only structural differences being briefly discussed. According to the calculation results based on density functional theory (DFT), all fluorinated ethers exhibit lower highest occupied molecular orbitals (HOMOs) compared to their non-fluorinated counterparts (Supplementary Fig. 5 and Supplementary Data 1–6), suggesting improved oxidation stabilities after fluorination.

μ is a measure of the polarity of the solvent molecule, which will not only significantly affect the coordination and solvation of Li^+ but also reflect the response of solvents to electric fields within electric double layer (EDL), where de-solvation, SEI formation, and adsorption of solvents on the electrode surface occur. Many studies have shown that ion-dipole interaction plays a critical role in solvation and de-solvation, interphase regulation and protection[25,34–36]. Generally, molecules with low μ exhibit poor sensitivity to the electric fields within EDL, resulting in sluggish de-solvation. Nevertheless, molecules with excessively high μ may lead to strong dissolution of interphase components[37]. Therefore, it is necessary to highlight molecules with moderate μ (1.5 ~ 3.5 Debye) holding great potential for facile de-solvation and interphase regulation. Despite having desirable μ values, there are some solvents [e.g., 1,1,2,2-tetrafluoroethyl-2,2,3,3-tetrafluoroprpyl ether (TTE)] that can barely dissociate the LiFSI salt, suggesting that other parameter besides μ value needs to be considered.

Usually, the oxygen atom of ether is the primary site to coordinate with Li^+, and its coordination ability determines the solvation ability of ether solvent. To quantify the coordination ability of oxygen atoms, $RESP_O$ was proposed as the other descriptor. RESP is a modified ESP method that incorporates physical constraints (e.g., atomic electronegativity equilibration and bond symmetry constraints) to optimize charge distributions, ensuring further improvement of the rationality of the charge model, which leads to more efficient and accurate distinction between ethers with different solvation abilities. Specifically, as the $RESP_O$ value increases (less negative), the solvation ability of oxygen decreases. The electrolyte solvents of LMBs are desired to have relatively weak solvation ability while providing sufficient solubility, where the solvents with moderately high $RESP_O$ values (−0.46 ~ −0.36 eV) can be screened out.

As shown in Fig. 1b, under the guidance of $RESP_O$–μ dual descriptors, TFPM, bis(2-fluoroethyl) ether (BFE), tetrahydrofuran (THF), and tetrahydropyran (THP) emerged as optimal solvents with good Li reversibility and kinetics among the designed solvents and other reported solvents[7,31,38–41]. Unfortunately, the poor oxidation stability of THF and THP solvents has hindered their application with high-voltage positive electrodes. BFE, a recently reported monofluoride ether with Li-F and Li-O tridentate coordination chemistries, demonstrates good compatibility with both high-voltage positive electrodes and Li-metal in a wide temperature range, validating the reliability of our solvent screening principle. Driven by weakened coordination ability of O and moderate μ, TFPM tends to form a stable six-membered chelating structure through Li-F and Li-O coordination (Fig. 1c), which is expected to bestow sufficient salt solubility, fast kinetics, and high interfacial stability even at low temperatures.

Fluorine coordination chemistry mediated chelating solvation structure

Prior to experimental validation, comprehensive theoretical investigations were conducted to explore the rationale of the dual descriptors-based selection principle. DFT calculations were initially employed to elucidate the binding geometries between diverse solvent molecules and Li^+. As shown in Fig. 2a–d, Supplementary Fig. 6, and Supplementary Data 7–12, the Li-O distance in TFPM is relatively large (1.853 Å), which is only slightly lower than that in TFEM (1.889 Å), reflecting the weak coordination effect of the O atom. Notably, TFPM exhibits the strongest Li-F interaction with the shortest Li-F distance of 1.845 Å, indicating the strong coordination tendency of F atom (on $-CF_3$) with Li^+, which leads to the formation of a stable six-membered chelating structure in Li^+–TFPM complexes with the most negative binding energy (−2.16 eV). Although the TFEM and TFBM molecules have higher μ that can induce stronger ion-dipole interactions, the larger tension of the five-membered and seven-membered rings leads to a decrease in the stability of the chelating structures, as indicated by less negative binding energies (Fig. 2d and Supplementary Fig. 6b). The synergistic O and F chelation is anticipated to boost the Li salt dissociation and mitigate the ionic conductivity reduction typically associated with fluorination.

NMR measurements were carried out to verify the coordination effect between solvent and Li^+. In ^7Li NMR spectra, higher chemical shift represents less shielding effect of Li nuclei, suggesting weak coordination of the surrounding ligands. As shown in ^7Li NMR in Fig. 2e, LiFSI/PM and LiFSI/BM electrolytes have larger chemical shifts compared to LiFSI/TFPM and LiFSI/TFBM electrolytes, which indicates a weaker solvation ability of PM and BM solvents. However, considering the synergistic coordination effect of O and F, further differentiation of coordination interaction was revealed through ^{17}O NMR (Fig. 2f) and ^{19}F NMR (Fig. 2g). For the LiFSI/TFPM electrolyte, minimal shift was observed in ^{17}O spectrum, while maximum shift was observed in the ^{19}F spectrum, indicating the weakest coordination ability of O and the strongest coordination ability of F in the TFPM solvent, which is well consistent with the DFT calculations (Fig. 2a–d). This Li-F and Li-O bidentate coordination effect significantly promotes the solvation ability of TFPM, leading to more shielding effect and lower chemical shift in ^7Li NMR spectrum.

The Li^+ solvation structure dominates the ionic transport, de-solvation, and SEI compositions, which was first investigated by molecular dynamics (MD) simulations (Supplementary Fig. 7 and Supplementary Data 13–16). According to the statistic results from MD, all electrolytes including 2 M LiFSI/PM, 2 M LiFSI/BM, 2 M LiFSI/TFPM, and 2 M LiFSI/TFBM possess anion-rich solvation structure, of which more than 95% first solvation sheath was dominated by two or more FSI^- anions (Fig. 3a–d), with the most probable solvation structure being 3 anions

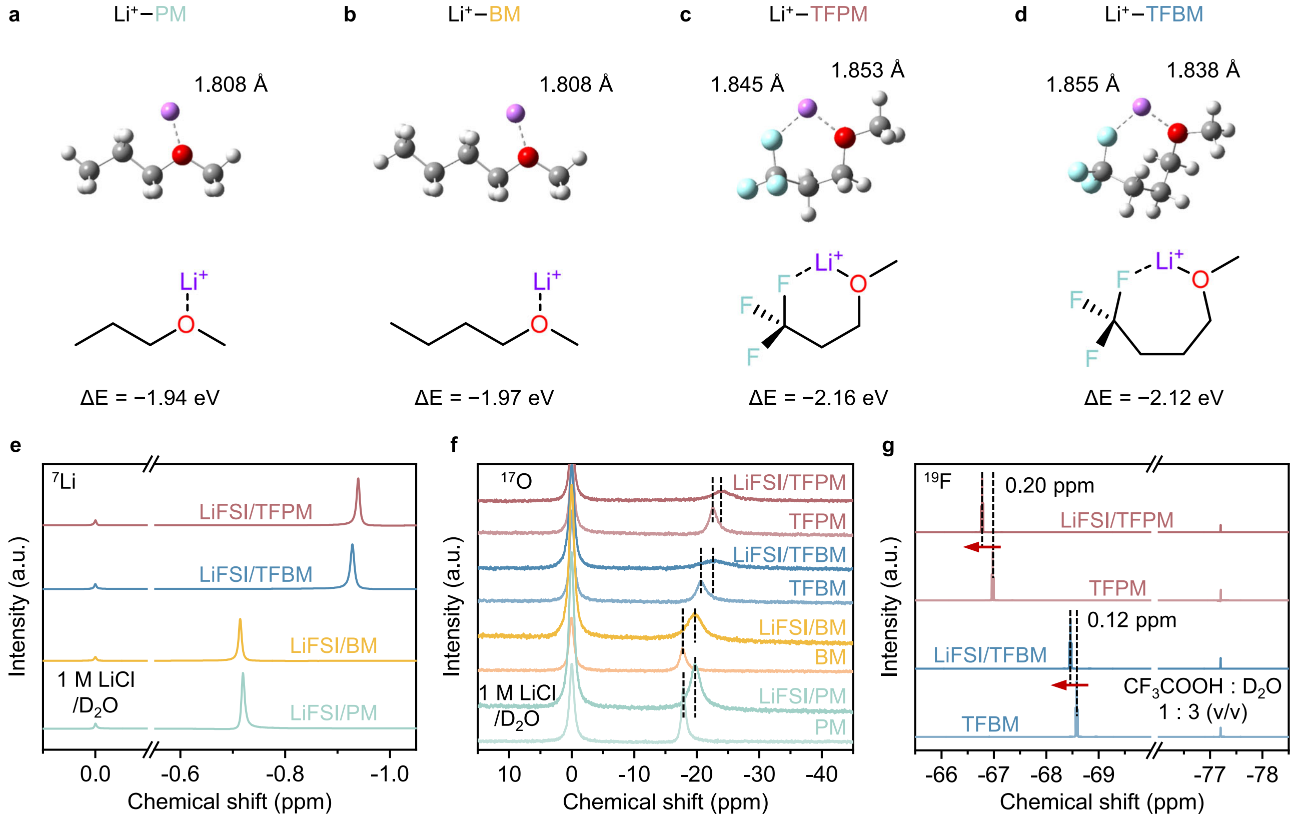

Fig. 2 | Coordination chemistries of solvents. a–d Coordination structures and their corresponding binding energies between one Li$^+$ and one solvent molecule. Purple, red, cyan, grey, and white spheres represent Li$^+$, O, F, C, and H, respectively. **e** ^{7}Li NMR spectra of various electrolytes. **f** ^{17}O and **g** ^{19}F NMR spectra of solvents before and after dissolving LiFSI salt. Source data are provided as a Source Data file.

and 1 solvent molecule coordinated with Li$^+$ (Supplementary Fig. 8 and Supplementary Data 17–20). To quantify the local environment around the Li$^+$ in various electrolytes, the radial distribution functions (RDFs) of both the anion and solvent with respect to Li$^+$ were calculated (Fig. 3e–h). Specifically, the average coordination number of the FSI$^-$ anion and solvent in the first solvation sheath (within 3 Å from Li$^+$) was calculated to be $Li^+(FSI^-)_{2.86}(PM)_{1.16}$, $Li^+(FSI^-)_{2.68}(BM)_{1.33}$, $Li^+(FSI^-)_{3.03}(TFPM)_{0.99}$, and $Li^+(FSI^-)_{2.93}(TFBM)_{1.08}$ for the 2 M LiFSI/PM, 2 M LiFSI/BM, 2 M LiFSI/TFPM, and 2 M LiFSI/TFBM electrolytes, respectively, of which the minimal coordination number of O in TFPM is consistent with the screening results of RESP$_O$. As shown in the Fig. 3i, the 2 M LiFSI/TFPM electrolyte exhibits a much higher FSI$^-$/solvent ratio (i.e., 3.06) than that of 2 M LiFSI/PM (i.e., 2.47), 2 M LiFSI/BM (i.e., 2.02), and 2 M LiFSI/TFBM (i.e., 2.71) in the primary solvation sheath.

The solvation structure in different electrolytes was further verified by Raman spectroscopy. The Raman band located between 690–780 cm^{-1} is corresponding to the stretching vibration peak of the S-N-S bond on FSI$^-$. As the position of this peak gradually upshifts, the coordination state of FSI$^-$ anion transforms from solvent-separated ion pairs (SSIPs) to contact ion pairs (CIPs), and then to aggregates (AGGs)[42]. As shown in Fig. 3j, the peak positions of S-N-S bond in four electrolytes are all greater than 745.0 cm^{-1}, reflecting the solvation structures of all electrolytes are dominated by AGGs, which is in good agreement with MD results. The peaks are centered at 745.6 cm^{-1} for PM and BM electrolytes, which upshifts to 752.2 cm^{-1} for TFBM electrolyte and further to 755.5 cm^{-1} for TFPM electrolyte, indicating enhanced anion coordination, which is favorable for promoting the formation of inorganic-rich SEI. Furthermore, the peak at about 804 cm^{-1} is assigned to the vibration of C−F bond of TFPM. This peak is broadened after dissolving LiFSI salt with the full width at half maxima (FWHM) increased from 21.0 cm^{-1} to 32.1 cm^{-1}, validating that partial F atoms on TFPM has been coordinated with Li$^+$, while no obvious FWHM change is observed for TFBM after dissolving salt.

According to the differential scanning calorimetry (DSC) curves, there is no phase change for all electrolytes even when the temperature was decreased to below −100 °C (Supplementary Fig. 9), indicating that the electrolytes will not be frozen, which is a prerequisite for operating the LMBs under low temperatures. Among the four investigated electrolytes, the 2 M LiFSI/TFPM electrolyte exhibits moderate ionic conductivities and viscosities at all measured temperatures range from −40 to 40 °C (Supplementary Figs. 10, 11). In addition, the average de-solvation energies (Avg. ΔE_{dsv}) of four electrolytes were calculated based on the solvation structures derived from MD results. As revealed in Fig. 3k, the 2 M LiFSI/TFPM electrolyte exhibits the lowest Avg. ΔE_{dsv} of 2.14 eV, outperforming that of 2 M LiFSI/PM (2.25 eV), 2 M LiFSI/TFBM (2.29 eV), and 2 M LiFSI/BM (2.62 eV), which is beneficial for facile de-solvation and homogeneous Li deposition. Therefore, the Li-F and Li-O bidentate coordination chemistries offered by TFPM solvent induces the formation of six-membered chelating structure in LiFSI/TFPM electrolyte, leading to the sufficient salt dissociation, reduced solvent number and enhanced Li$^+$−FSI$^-$ pairing in the solvation sheath, which not only facilitates ion transport and de-solvation but also will contribute to formation of highly conductive inorganic-rich SEI.

Highly reversible Li plating/stripping from 30 to −60 °C

The compatibility of the TFPM electrolyte was systematically evaluated in Li||Cu asymmetric cells. As shown in Fig. 4a, with the modified Aurbach method[43], the TFPM electrolyte can offer a high CE up to 99.6%, which is better than that of PM (99.3%), BM (99.3%), and TFBM (99.1%) electrolytes at a current density of 1.0 mA cm^{-2} for 1.0 mAh cm^{-2} at 30 °C. To examine the Li deposition morphology in various electrolytes, 5.0 mAh cm^{-2} of Li metal was plated on the bare

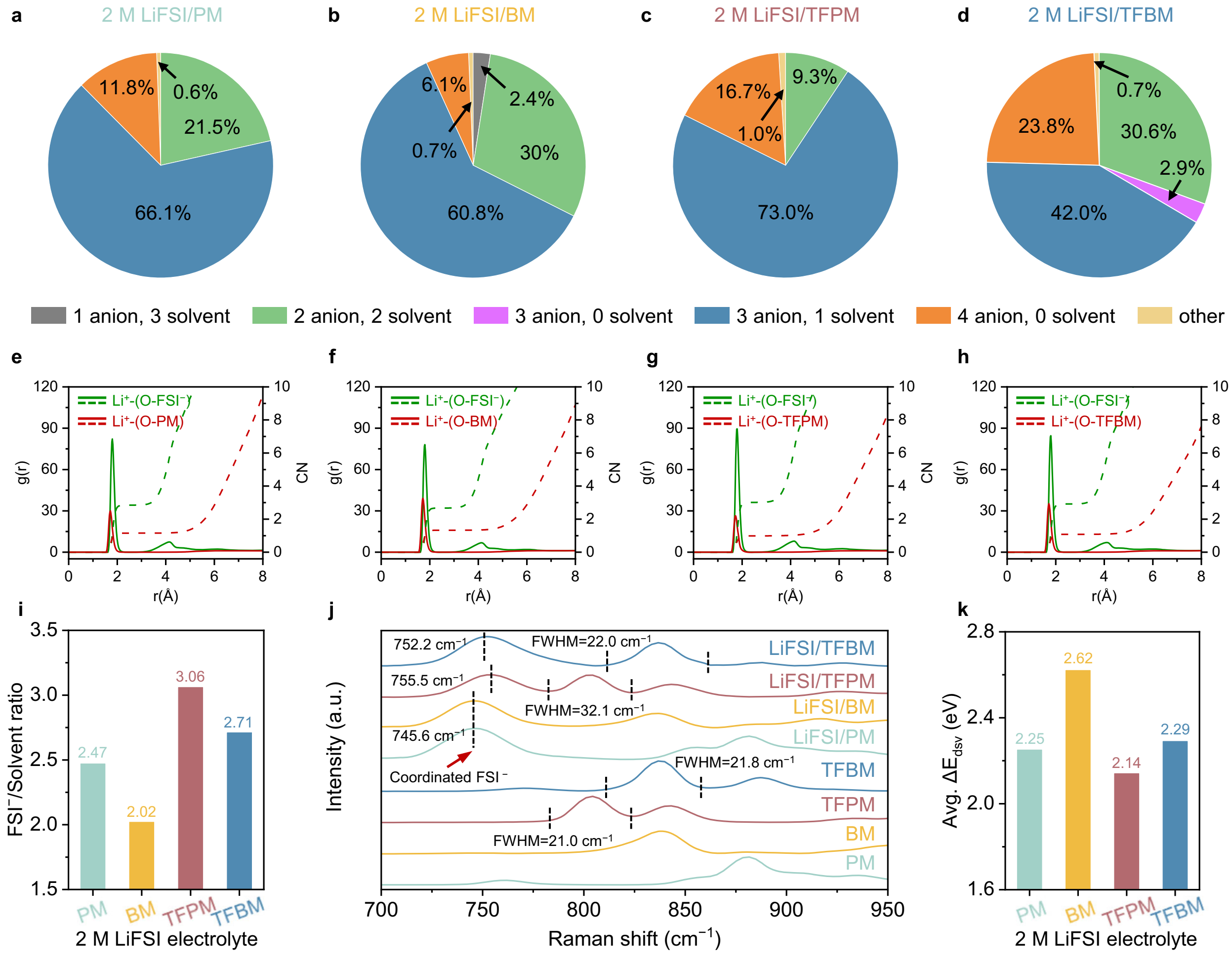

Fig. 3 | Theoretical and experimental studies of Li$^+$ solvation structures. Distributions of primary solvation sheath compositions of **a** 2 M LiFSI/PM, **b** 2 M LiFSI/BM, **c** 2 M LiFSI/TFPM, and **d** 2 M LiFSI/TFBM electrolytes based on MD simulations. Radial distribution functions (RDFs) calculated from MD simulations of **e** 2 M LiFSI/PM, **f** 2 M LiFSI/BM, **g** 2 M LiFSI/TFPM, and **h** 2 M LiFSI/TFBM electrolytes. **i** FSI$^-$/solvent ratio in the first solvation sheath (within 3 Å from Li$^+$) of electrolytes. **j** Raman spectra of the 2 M LiFSI electrolytes and their solvents. **k** Average de-solvation energy (Avg. ΔE$_{dsv}$) of different electrolytes. Source data are provided as a Source Data file.

Cu foils. As shown in the scanning electron microscopy (SEM) images in Supplementary Fig. 12, particle-like Li deposits with many pores are observed in PM, BM, and TFBM electrolytes, which may induce the over-decomposition of the electrolyte and result in the accumulation of thick SEI. In sharp contrast, highly compact and smooth Li deposition was achieved in TFPM electrolyte, which is beneficial for minimizing the parasitic reaction and inhibiting the formation of dead Li during long-term cycling.

Long-term cycling of Li||Cu cells further highlights the advantages of TFPM electrolyte. As shown in Fig. 4b, the cells using PM, BM, and TFBM electrolytes exhibit fluctuating CE during cycling, leading to cells failure within 440 cycles. Among these three electrolytes, the PM electrolyte delivers a relatively high average CE of 99.2% within 400 cycles, which can be attributed to its high ionic conductivity (Supplementary Fig. 10) and relatively low de-solvation energy (Fig. 3k). Notably, TFPM electrolyte demonstrates stable cycling for over 850 cycles with a high average CE of 99.3%, representing the pioneering work for "single salt single solvent" electrolytes reported thus far at a relatively high current density of 1.0 mA cm^{-2} (Supplementary Table 2), which is not only attributed to its low de-solvation energy but also the moderate μ of TFPM that holds sufficient sensitivity to the electric fields while maintaining the interphase integrity simultaneously. As shown in Supplementary Fig. 13, owing to its rapid electrochemical kinetics and enhanced interfacial stability, the Li plating/stripping profiles of Li||Cu cell using TFPM electrolyte delivers the lowest initial overpotential and smoothest evolution during cycling.

The operational advantages of TFPM electrolyte become more pronounced at low temperatures. As shown in Fig. 4c, when the temperature was reduced to −40 °C, the CE of Li||Cu cells using PM, BM, and TFBM electrolytes sharply drops to 93.3%, 95.5%, and 97.0%, respectively, with highly porous Li deposit morphologies (Fig. 4e). Whereas, the TFPM electrolyte still retains a high CE of 98.7% even at a high current density of 1.0 mA cm^{-2}, which is competitive compared to state-of-the-art reported electrolytes under such high current densities (Supplementary Table 3). The SEM image and photograph reveal that the TFPM electrolyte still bestows highly dense and smooth Li deposits with a shiny silver appearance (Fig. 4e). When the temperature was further dropped to −60 °C, the cells using PM and BM electrolytes exhibit abnormal voltage profiles during Li plating/stripping (Fig. 4d), and the Li metal was barely deposited on Cu foils with obvious dendrites formation (Fig. 4f). For the cell using TFBM, despite delivering smooth Li plating/stripping profiles, it was found that CE dropped dramatically to 91.7% with dark and non-uniform Li deposits (Fig. 4f). Extraordinarily, the cell using the TFPM electrolyte still maintains a high CE of 96.1% (Fig. 4d) and yields uniform Li deposition morphology with silver appearance (Fig. 4f), demonstrating the effectiveness of TFPM electrolyte in enabling highly reversible Li plating/stripping at low temperatures.

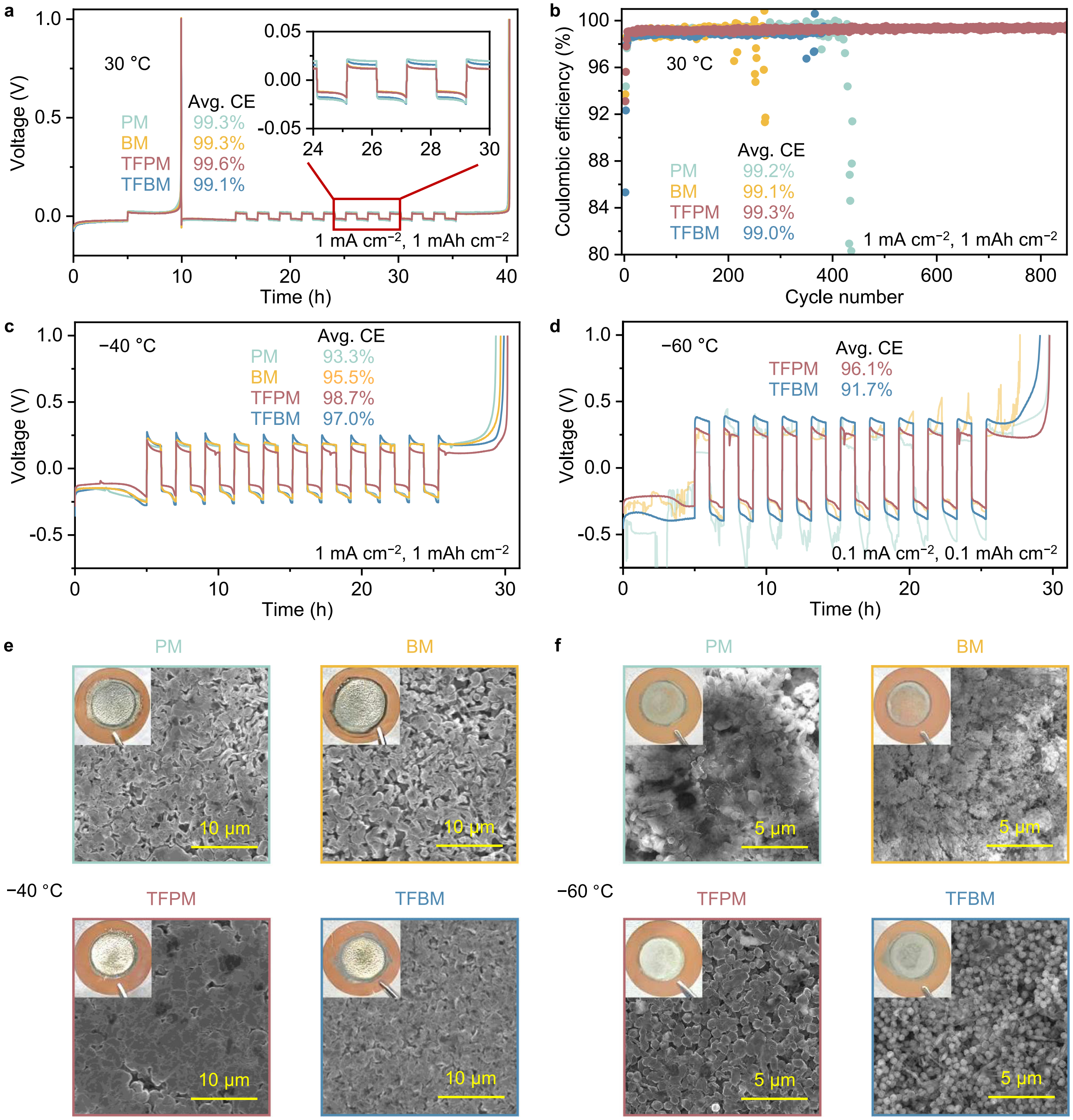

Fig. 4 | Li metal reversibility and deposition morphology. **a** Modified Aurbach measurement and **b** cycling test of Li||Cu cells at 30 °C with a current density of 1.0 mA cm^{-2} for 1.0 mAh cm^{-2}. Modified Aurbach measurement of Li||Cu cells at **c** −40 °C with a current density of 1.0 mA cm^{-2} for 1.0 mAh cm^{-2} and **d** −60 °C with a current density of 0.1 mA cm^{-2} for 0.1 mAh cm^{-2}. SEM images and corresponding optical photographs of Cu foils using different electrolytes after plating **e** 5.0 mAh cm^{-2} of Li metal at −40 °C (Scale bar = 10 μm) and **f** 2.0 mAh cm^{-2} of Li metal at −60 °C (Scale bar = 5 μm). Source data are provided as a Source Data file.

Fast electrochemical kinetics and high interfacial stability

In addition to the ionic conductivity and de-solvation process, the compositions of SEI play a vital role for the Li$^+$ migration and subsequent Li deposition behavior. Thus after 10 cycles of Li plating/stripping in Li||Cu cells with different electrolytes, X-ray photoelectron spectroscopy (XPS) analysis with etching depth profiles was applied to study the SEI components and their distributions on Li metal in various electrolytes. As shown in Fig. 5a and Supplementary Fig. 14, the atomic ratio of C for PM (63.5%) and BM (60.7%) electrolytes is much higher than TFPM (43.0%) and TFBM (37.3%) electrolytes, which remains consistently high for PM and BM electrolytes even after 240 s of Ar$^+$ sputtering, but is significantly reduced for TFPM and TFBM electrolytes. The C 1*s* spectra with depth profiles also show much higher peak intensities for the PM and BM electrolytes (Supplementary Fig. 15), which is an indication of rich in organic components for the SEI. On the other hand, inorganic components represented by the atomic ratio of F ranks as TFBM (8.4%) > TFPM (7.7%) > PM (6.4%) > BM (3.7%). While in the F 1*s* spectra (Fig. 5b), the LiF peak intensity, reflecting the absolute F content, is much higher for TFPM than TFBM electrolyte. This indicates that the SEI formed in the TFBM electrolyte may be dissolved out by the TFBM solvent with high μ value, leading to less SEI residues on the surface of Li metal, as demonstrated by previous publications[36,37], which may cause continuous electrolyte decomposition during prolonged cycling. According to the N 1*s*, S 2*p*,

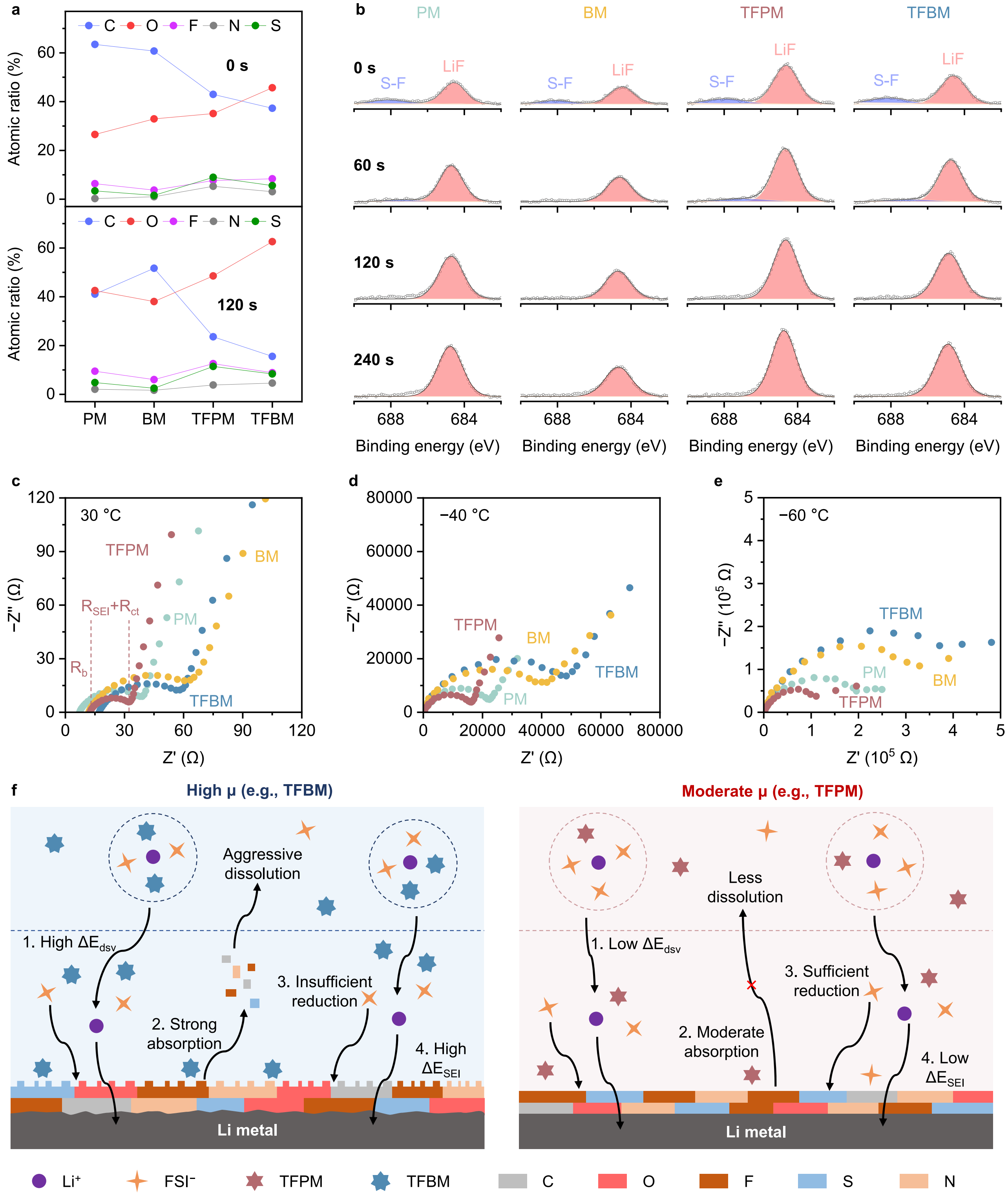

Fig. 5 | Analysis of electrochemical kinetics and interphases. a Atomic ratio of the SEI on Li metal before and after 120 s of sputtering. **b** F 1*s* XPS spectra of Li metal at different time of Ar^+ sputtering. The Li metal plated on Cu foil was collected from Li||Cu cells after 10 cycles of Li plating/stripping in different electrolytes at 1.0 mA cm^{-2} for 1.0 mAh cm^{-2} at 30 °C. EIS spectra of Li||Cu cells after 10 cycles with a current density of 1.0 mA cm^{-2} for 1.0 mAh cm^{-2} at **c** 30 °C, **d** −40 °C, and **e** −60 °C. **f** Schematic illustrations of electrochemical kinetics and interphase formation in the electrolytes with high μ or moderate μ solvent. Source data are provided as a Source Data file.

and O 1*s* spectra shown in Supplementary Figs. 16–18, more FSI^- anions were decomposed in TFPM and TFBM electrolytes to generate inorganic SEI components. It is worth noting that more LiN_xO_y and Li_2S_x, the thorough decomposition products of FSI^- anion, were detected for TFPM electrolyte, building up inorganic-rich SEI that is highly stable with low resistance.

To clarify the vital impact of μ on the interphase stability, the electrochemical quartz crystal microbalance (EQCM) was employed to monitor the gravimetric variation of SEI in-situ[44–46]. As shown in the Supplementary Fig. 19, after 300 s of discharge, a high mass of 13,170 ng cm^{-2}, corresponding to the plated Li with SEI layer, is generated in the BM electrolyte. During the subsequent resting process, the SEI formed by BM electrolyte slowly dissolves at a rate of 6.6 ng s^{-1} cm^{-2} due to the low dissolution ability of BM solvent (low μ). The initial plated Li with SEI layers formed by TFPM and TFBM electrolytes show similar mass. However, the SEI dissolves rapidly in the TFBM electrolyte at a high rate of 20.9 ng s^{-1} cm^{-2} due to the high μ of TFBM, whereas a moderate dissolution rate of 9.3 ng s^{-1} cm^{-2} was found for the TFPM electrolyte, facilitating the formation of a robust inorganic-rich SEI. Moreover, the TFPM electrolyte also shows substantially higher exchange current density compared to the other three electrolytes at both 30 °C and −40 °C (Supplementary Figs. 20, 21), demonstrating its high sensitivity to the electric fields that promotes Li plating/stripping kinetics. This validates that the TFPM solvent with moderate μ could achieve a good balance between sensitivity to the electric fields within EDL and interphase stability.

To reveal the effect of different solvents on Li plating behavior, the electrochemical impedance spectra (EIS) were recorded for Li||Cu cells after 10 cycles. The impendences can be divided into bulk resistance (R_b), charge transfer resistance (R_{ct}), and SEI resistance (R_{SEI}), which describes the processes of Li^+ transport in bulk electrolyte, desolvation of solvated Li^+, and migration of Li^+ through SEI, respectively. As shown in Fig. 5c, at 30 °C, the R_b trend of various cells is well-accorded with the ionic conductivities of various electrolytes. Looking into the semi-cycle region of EIS spectra, it is found that TFPM electrolyte with moderate μ exhibits much lower total resistance of R_{SEI} and R_{ct} compared to the other three electrolytes, validating its much lower SEI resistance and de-solvation energy, which is highly desirable for high-rate operation of LMBs. When the temperature decreases sequentially from 30 °C to −20 °C, −40 °C and −60 °C (Fig. 5d, e, Supplementary Fig. 22), the advantages of TFPM electrolyte are further amplified with substantially lower total resistance ($R_b + R_{SEI} + R_{ct}$) than the other three, holding great potential for operating LMBs at low temperatures.

Based on the above discussions, it should be noted that two asymmetric fluorinated ethers (i.e., TFPM and TFBM), with only one methylene group difference in chemical structure, exhibit dramatic difference in Li deposition behavior. As schematically illustrated in Fig. 5f, the TFPM electrolyte is better than the TFBM electrolyte in the following aspects: (1) due to the weakened coordination ability of O and F-mediated coordination effect, TFPM solvent induces a stable six-membered chelating solvation structure with highly rich in anion, resulting in low de-solvation energy while maintaining sufficient salt dissociation; (2) the TFBM electrolyte exhibits lower ionic conductivity and higher viscosity compared to the TFPM electrolyte, hindering efficient ion transport, especially under high-rate and low-temperature conditions; (3) the TFBM solvent with high μ tends to adsorb on the surface of Li-metal strongly, leading to the aggressive dissolution of interphase components, while the TFPM solvent with moderate μ could achieve a balance between sensitivity to the electric fields within EDL and interphase protection; (4) because of the strong dissolution ability of TFBM solvent, FSI^- anions do not have enough time to decompose before being dissolved out, resulting in insufficient anion reduction; (5) since the "interphase dissolution−electrolyte decomposition" process is constantly going on in the TFBM electrolyte, the interphase is in a highly dynamic evolution, which yields highly unstable SEI with large resistance. While the TFPM with moderate μ enables sufficient reduction of FSI^- anions, leading to the formation of highly robust inorganic-rich SEI with low resistance. These merits significantly enhance the electrochemical kinetics and interfacial stability for Li-metal electrode, which are beneficial for enabling high-energy and low-temperature LMBs.

Full cell and pouch cell evaluation at benign and low temperatures

To build high-energy LMBs, the electrolyte must possess high anodic stability to match the high-voltage positive electrodes such as NMC811 or NMC9055. Linear sweep voltammetry (LSV) with Al as working electrode was performed to evaluate the anodic stability of four electrolytes. As shown in Supplementary Fig. 23, the current quickly rise to 3 μA cm^{-2} at 3.7 V for the BM electrolyte, which may be ascribed to the Al corrosion and/or oxidation decomposition of the BM solvent. The current leakage was postponed to 4.5 V for PM electrolyte, which was attributed to its weakened solvation ability that barely solvate Al^{3+}, thereby inhibiting the Al corrosion to a certain extent. While for two fluorinated electrolytes (i.e., TFPM and TFBM), no obvious current leakage was observed until 5.5 V, demonstrating their enhanced anodic stability. The chronoamperometry (CA) test of Li||Al cells further validates this phenomena, high leakage current was found for BM electrolyte when holding at 4.5 V (Supplementary Fig. 24a). Furthermore, the SEM image shows obvious corrosion spots on Al surface after 24 h of holding (Supplementary Fig. 24b). In contrast, the PM, TFPM, and TFBM electrolytes show no Al corrosion and negligible leakage current with the TFPM electrolyte being the lowest. Moreover, to further testify the anodic stability of the electrolytes in practical batteries, the electrochemical floating test of Li||NMC811 cells using different electrolytes were carried out. As shown in Fig. 6a, the cell using BM electrolyte exhibits obvious increase in leakage current when elevating the voltage to 4.4 V, of which the leakage current further exceeds 100 μA cm^{-2} at 4.5 V, indicating severe parasitic reaction occurs. This suggests that the BM electrolyte is inapplicable for high-voltage positive electrodes, which was excluded for practical battery evaluation. Similarly, the TFPM electrolyte demonstrates the highest oxidation stability with negligible leakage current, validating its great feasibility for high-voltage operation.

Owing to its advantages in Li-metal compatibility, electrochemical kinetics, and high-voltage tolerance, the TFPM electrolyte was applied to the high-voltage LMBs with Ni-rich NMC positive electrodes. As shown in Fig. 6b and Supplementary Fig. 25, under a high cut-off voltage of 4.4 V, the Li||NMC811 cell using the TFPM electrolyte shows good rate performance from 0.1 C to 20 C at 30 °C, which still delivers a high specific capacity of 127.1 mAh g^{-1} with low voltage polarization even at 20 C, significantly outperforming that of PM (96.3 mAh g^{-1}) and TFBM (34.6 mAh g^{-1}) electrolytes. This is attributed to the rapid de-solvation process and low ΔE_{SEI} offered by TFPM electrolyte. Long-term cycling performance of Li||NMC811 cells were first evaluated at 2.0 C. As shown in Fig. 6c and Supplementary Fig. 26, the Li||NMC811 cell using TFPM exhibits very stable cycling performance with a high specific capacity of 83.3% and a high average CE of 99.8% after 600 cycles. Considering its good rate capability, we then further test the cell at a high rate of 5.0 C, of which the high-power output is desirable for electric vertical take-off and landing (eVTOL) scenarios. As shown in Fig. 6d and Supplementary Fig. 27, the Li||NMC811 cell with TFPM electrolyte demonstrates a stable cycling performance with 81.0% capacity retention and a high average CE of 99.9% after 900 cycles. This can be attributed to the fast electrochemical kinetics and interphase protection ability provided by TFPM, which not only effectively promotes the Li^+ transport, de-solvation, and Li deposition, but also inhibits the side reaction during cycling. Because of the high anodic stability and relatively rich inorganic components in SEI, the TFBM electrolyte can also support the operation 900 cycles, but with a lower capacity retention of 68.0%. More importantly, the TFPM electrolyte also enables the stable cycling of even aggressive Li||NMC9055 cell for more than 750 cycles at 2.0 C (Supplementary Figs. 28, 29).

To mimic the realistic assembly of LMBs for practical application, 50 μm thin Li foil and high areal capacity NMC811 positive electrode (4.0 mAh cm^{-2}) were adopted to assemble the Li||NMC811 coin cells,

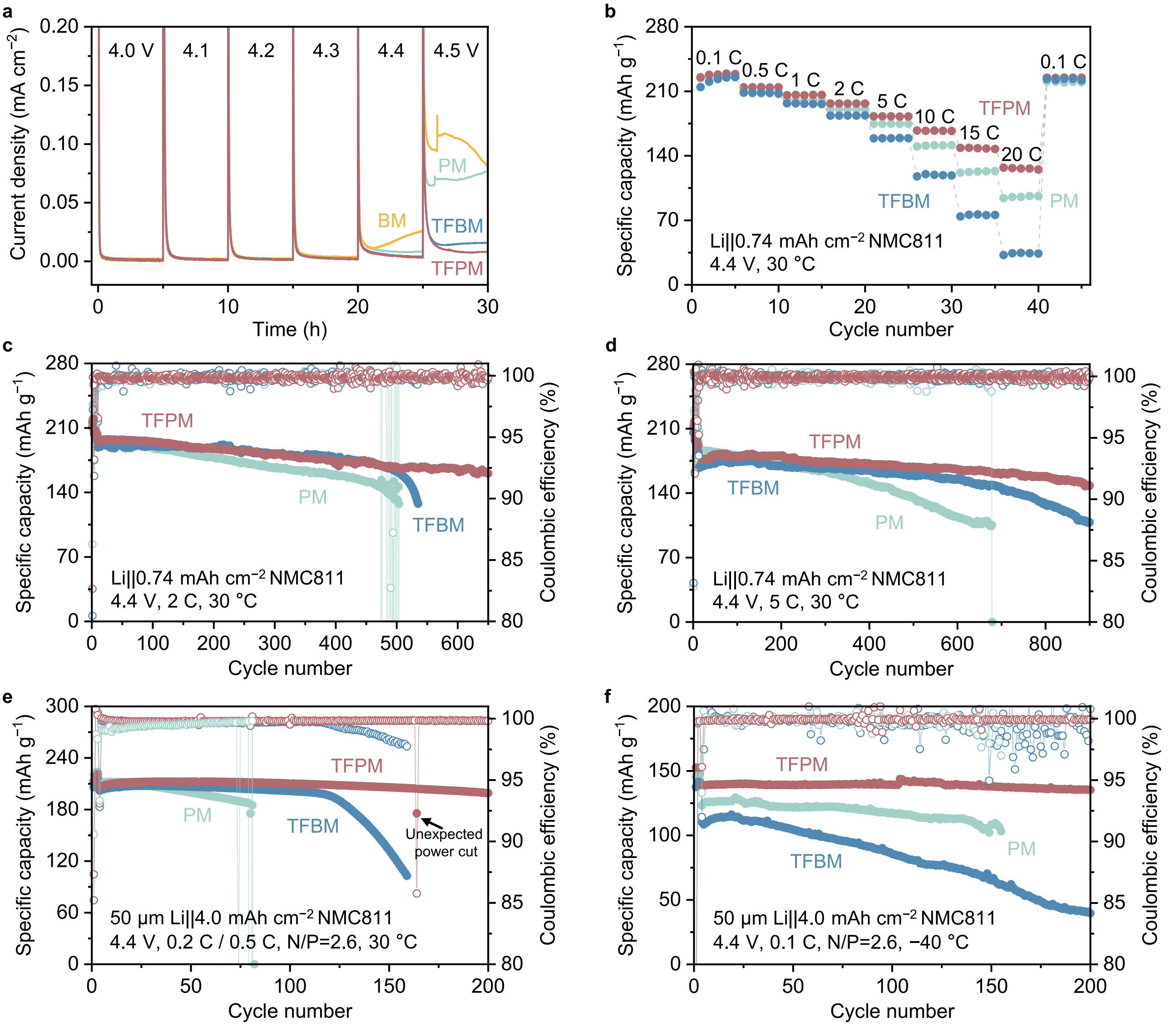

Fig. 6 | Electrochemical performance of Li | |NMC811 coin cells. a Electrochemical floating test of the electrolytes on a NMC811 electrode from 4.0 to 4.5 V. **b** Rate performance of the Li | |NMC811 cells at 30 °C, 1 C = 210 mA g^{-1}. Cycling performance of the Li | |NMC811 cells at **c** 2.0 C and **d** 5.0 C at 30 °C. Cycling performance of the Li | |NMC811 cells with thin Li-metal (50 μm) and a high areal capacity NMC811-positive electrode (4.0 mAh cm^{-2}) at **e** 30 °C with 0.2 C charge/0.5 C discharge and **f** −40 °C with 0.1 C charge/discharge. Source data are provided as a Source Data file.

leading to a practically low negative to positive electrode capacity (N/P) ratio of 2.6. As presented in Fig. 6e, at 30 °C, the cell with PM electrolyte suffers obvious short circuit with a short life-span of only 80 cycles (Supplementary Fig. 30a), which is ascribed to the uneven Li deposition that leads to the growth of Li dendrites. While the cell using TFBM electrolyte exhibits stable cycling during the first 120 cycles and then undergoes rapid capacity decay, which is due to the highly dynamic evolution of the SEI caused by the TFBM solvent with high μ, leading to the depletion of the limited electrolyte and Li metal. In stark contrast, the cell using TFPM electrolyte demonstrates a high capacity retention of 93.7% after 200 cycles with a high average CE of 99.8%. In addition, the charge-discharge profiles do not show obvious increase in voltage polarization during cycling, indicating its high interfacial stability (Supplementary Fig. 30b).

To further highlight the advantages of TFPM electrolyte, the cell was then tested at low temperatures. As shown in Fig. 6f and Supplementary Fig. 31, when the temperature was dropped to −40 °C, the cell using the TFPM electrolyte still displays a high specific capacity of 143.7 mAh g^{-1} and enables stable cycling at 0.1 C for 200 cycles, with a capacity retention of 94.1% and a high average CE of 99.9%. In contrast, due to the poor ionic conductivity and high viscosity of the TFBM electrolyte that leads to severe concentration polarization, the cell using TFBM electrolyte only delivers an initial specific capacity of 116.1 mAh g^{-1}. Furthermore, its unstable and dynamic interphase also results in rapid capacity decay with only 32.2% capacity retained after 200 cycles. Furthermore, owing to the high conductivity, low viscosity, and low de-solvation energy of PM electrolyte, the cell using PM electrolyte could release higher capacity than that using TFBM, but the organic-rich SEI results in the formation of dendritic and dead Li, making it unable to support long-term cycling. Considering thin Li-metal (50 μm) and high loading positive electrode (4.0 mAh cm^{-2}), the cycling life advantage for TFPM electrolyte is very obvious at low-temperature (≤ −20 °C) in comparison with other reported electrolytes (Supplementary Table 4). Besides, the cell using TFPM electrolyte also demonstrates good rate performance even at −40 °C (Supplementary Fig. 32). Notably, the TFPM electrolyte is still able to sustain the stable cycling of cell for more than 150 cycles at a very low temperature of −60 °C with an initial specific capacity of 116.5 mAh g^{-1} (Supplementary Fig. 33).

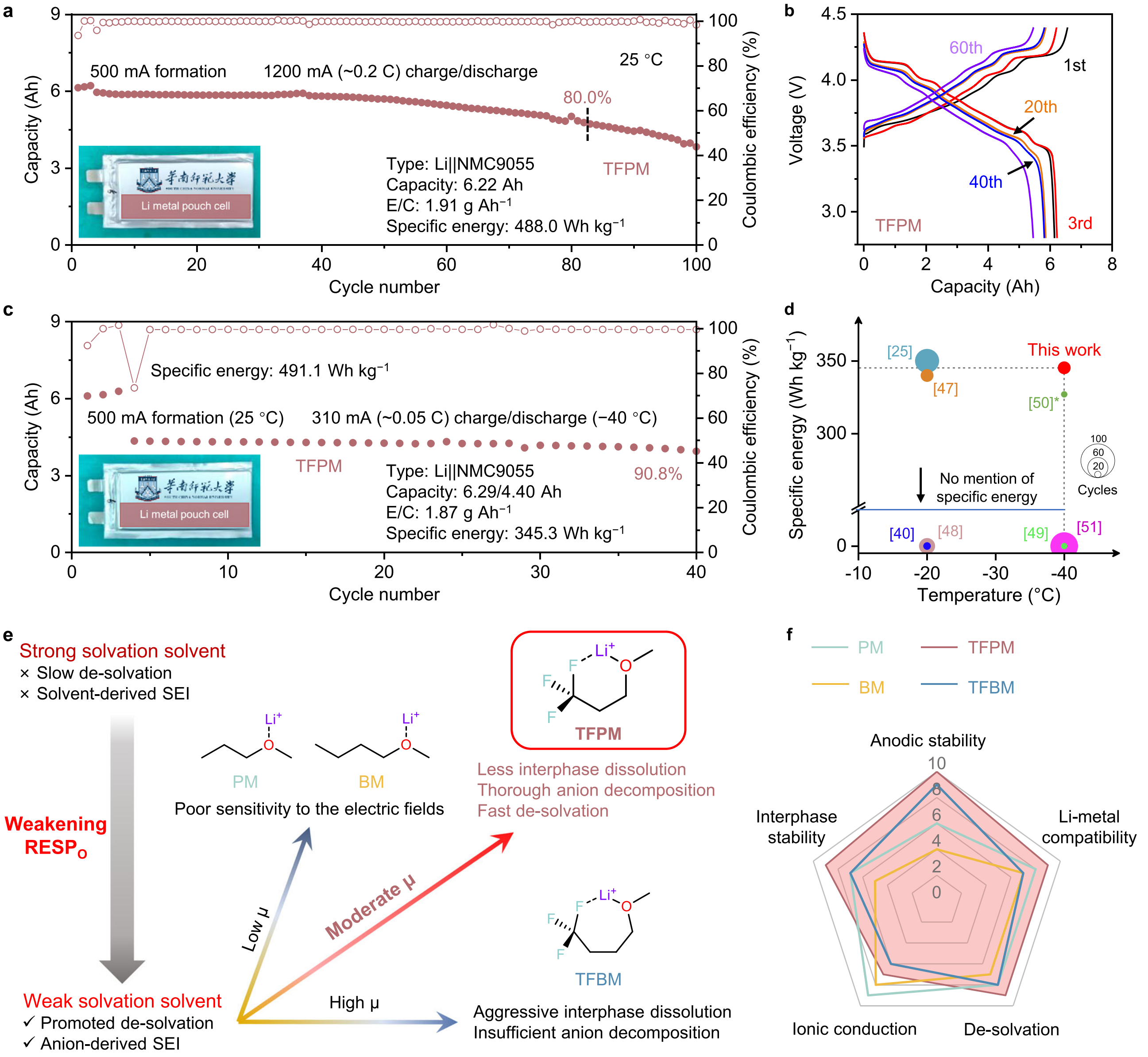

Fig. 7 | Evaluation of practical Li-metal pouch cells and the summary of this work. **a** Cycling performance and **b** charge-discharge profiles of the Li||NMC9055 pouch cell with the TFPM electrolyte at 25 °C. **c** Cycling performance of the Li||NMC9055 pouch cell with the TFPM electrolyte at −40 °C. **d** Comparison of this work with state-of-the-art reported Li-metal pouch cells at low temperatures (≤ −20 °C). The source of the literature data shown in this figure can be found in Supplementary Information Table 7[25,40,47–51]. Note: * represents excluding the weight of tabs and packing foil when calculating the specific energy. **e** Scheme showing the screening principle to balance the de-solvation and interphase stability in weak solvation solvent. **f** Radar plot with five aspects to evaluate the designed electrolytes. Ratings of 0 to 10 are given to each electrolyte (10 stands for ideal properties). Rationale for radar plot can be found in Supplementary Information Table 8. Source data are provided as a Source Data file.

The advantages of the TFPM electrolyte were eventually subjected to the test of Li-metal pouch cells. To achieve a high specific energy of ~500 Wh kg^{-1}, all parameters of the battery need to be strictly controlled. To reach this demand, a ~ 6.2 Ah level Li||NMC9055 pouch cell with lean electrolyte (1.91 g Ah^{-1}) and a low N/P ratio of 1.0 was assembled. The detailed parameters are shown in Supplementary Table 5, and the specific energy is calculated based on the mass of all components in the pouch cell. As shown in Fig. 7a, the pouch cell delivers the highest discharge capacity of 6.22 Ah at the third formation cycle, corresponding to a high specific energy of 488.0 Wh kg^{-1}. Furthermore, the pouch cell is able to retain over 80% capacity after 82 cycles with low voltage polarization (Fig. 7b). Given the good performance of the Li-metal coin cells at low temperatures (Fig. 6 and Supplementary Fig. 33), we further evaluate the electrochemical performance of pouch cell at −40 °C. Another pouch cell with initial capacity of 6.29 Ah (491.1 Wh kg^{-1}, based on the mass of all components with detailed parameters shown in Supplementary Table 6) at room temperature is able to deliver a capacity of 4.40 Ah at −40 °C, corresponding to 70% capacity at room temperature (Fig. 7c and Supplementary Fig. 34). This yields a high specific energy of 345.3 Wh kg^{-1} (based on the mass of all components) at such low temperature (i.e., −40 °C). What is more encouraging is that the pouch cell can be stably cycled for more than 40 cycles with a high capacity retention of 90.8% (Fig. 7c). In comparison with some relevant reported low-temperature pouch cells[25,40,47–51], our study stands out in terms of the highest specific energy and longest cycles at such low temperature (Fig. 7d and Supplementary Table 7).

Design overview and electrolyte merits

As illustrated in Fig. 7e, weakening the solvation ability of the solvent not only promotes the de-solvation process but also intensifies the Li^+–anion pairing to facilitate the formation of anion-derived inorganic-rich SEI. However, excessively weakening the solvation ability will result in low ionic conductivity, and not all weak solvation solvents could lead to better electrochemical kinetics and Li reversibility. Therefore, the structure of the solvent must be regulated carefully. In this study, the restrained electrostatic potential (RESP) of the coordinated O (denoted as $RESP_O$) was proposed as one descriptor to measure the solvation ability of ether solvents, and the dipole moment (μ) was proposed as correction descriptor to balance its sensitivity to the electric fields and interphase stability. Specifically, weak solvation solvent with low μ (e.g., PM and BM) exhibits poor sensitivity to the electric fields within EDL, which results in sluggish de-solvation. While the solvent with high μ (e.g., TFBM) tends to adsorb on the surface of Li-metal strongly, which leads to the aggressive dissolution of interphase components and insufficient anion decomposition, yielding highly unstable SEI with large resistance. As a rationale, the solvent with moderate μ (e.g., TFPM) possesses less dissolution ability to enable thorough anion decomposition, building highly stable SEI while maintaining fast de-solvation kinetics. Under the guidance of $RESP_O$–μ dual descriptors, despite possessing slightly lower ionic conductivity, the TFPM electrolyte stands out in the aspects of interphase stability, de-solvation, Li-metal compatibility, and anodic stability (Fig. 7f and Supplementary Table 8), which enables the stable operation of high-energy LMBs at low temperatures.

Discussion

In summary, a class of asymmetric ethers was rationally designed to enable high-energy LMBs at low temperatures. The restrained electrostatic potential of the coordinated O ($RESP_O$) was proposed as one descriptor to quantify the solvation effect of the ethers, followed by introducing the dipole moment (μ) as correction descriptor to optimize solvents' sensitivity to the electric fields and interphase stability. The systematic theoretical and experimental studies have demonstrated that the TFPM solvent with moderate $RESP_O$ and μ mediates a stable six-membered chelating structure with Li^+ through Li-F and Li-O bi-coordination, which not only reduces the de-solvation energy for rapid charge transfer but also builds a highly stable and conductive inorganic-rich SEI, significantly promoting the electrochemical kinetics and Li reversibility from 30 to −60 °C. Consequently, this single-salt single-solvent TFPM electrolyte promises the 50 μm Li||4.0 mAh cm^{-2} NMC811 coin cells to operate stably at benign and low temperatures for more than 200 cycles, retaining 93.7% capacity with 99.8% CE at 30 °C and 94.1% capacity with 99.9% CE at −40 °C, respectively. Most notably, a practical Li-metal pouch cell (6.29 Ah) with a specific energy of 491.1 Wh kg^{-1} is able to maintain a high specific energy of 345.3 Wh kg^{-1} at a low temperature of −40 °C, and can be stably cycled for 40 cycles with 90.8% capacity retention at this temperature. This work demonstrates the importance in tailoring coordination structures of electrolytes and provides a highly effective strategy for rational electrolyte solvent screening towards practical high-energy LMBs at low temperatures.

Methods

Materials

N-propyl methyl ether (PM, >95%) and n-butyl methyl ether (BM, >98%) were purchased from Tokyo Chemical Industry Co., Ltd. 2,2,2-trifluoroethanol (99.5%), 3,3,3-trifluoro-1-propanol (98%), 4,4,4-trifluoro-1-butanol (97%), iodomethane (MeI, 99.5%), and sodium hydride (NaH, 60% in mineral oil) were purchased from Energy Chemical. $LiNi_{0.8}Mn_{0.1}Co_{0.1}O_2$ (NMC811) was kindly provided by Guangzhou Tinci Materials Technology Co. Ltd. Lithium bis(fluorosulfonyl)imide (LiFSI, >99.9%) was purchased from Nippon Shokubai Co., Ltd. The separator (Celgard 2500, 25 μm thick, 55% porosity, and 0.064 μm average pore size) was purchased from Celgard, LLC. Li foil (99.95%, 500 μm thick), composite metal strip (50 μm Li foil + 8 μm Cu foil), Cu foil, Al current collector, and CR 2032-type coin cell cases were purchased from Guangdong Canrd New Energy Technology Co. Ltd. $LiNi_{0.9}Mn_{0.05}Co_{0.05}O_2$ (NMC9055) powders and the Li-metal pouch cells (6.2 Ah) without injecting electrolyte were purchased from Guangzhou Science Technology Co. Ltd.

Synthesis

The synthesis route is shown in the Supplementary Fig. 1. As a typical procedure, NaH (12.0 g, 60 wt.% in mineral oil, 0.30 mol) and 240 mL anhydrous DMF were added to a 500 mL two-necked round-bottom flask, the mixture was cooled to 0 °C. Then, 0.20 mol 2,2,2-trifluoroethanol (or 3,3,3-trifluoro-1-propanol or 4,4,4-trifluoro-1-butanol) was slowly added. Thereafter, the reaction was returned to room temperature for 30 min. Later, MeI (27.6 g, 0.24 mol) was slowly added at 0 °C, and the reaction was returned again to room temperature for 16 h. After reaction, 30 mL deionized water was slowly added to quench the reaction. The crude product was obtained by distilling the mixture under proper temperature. Then, the crude product was washed twice with 1.0 mol/L NaOH aqueous solution, saturated NaCl aqueous solution, and 1.0 mol/L HCl aqueous solution in sequence, of which the organic phase was retained after each wash. The obtained organic phase was distilled triple to yield the final product. Yield: ~70%.

TFEM: ^1H NMR (600 MHz, $CDCl_3$, δ/ppm): 3.77 (q, 2H), 3.52 (s, 3H). ^{19}F NMR (564 MHz, $CDCl_3$, δ/ppm): −74.20 (t, 3 F). ^{13}C NMR (150 MHz, $CDCl_3$, δ/ppm): 126.78-121.23, 69.91-69.24, 59.81.

TFPM: ^1H NMR (600 MHz, $CDCl_3$, δ/ppm): 3.60 (t, 2H), 3.37 (s, 3H), 2.43-2.36 (m, 2H). ^{19}F NMR (564 MHz, $CDCl_3$, δ/ppm): −64.90 (t, 3 F). ^{13}C NMR (150 MHz, $CDCl_3$, δ/ppm): 128.87-123.38, 65.22-65.16, 58.40, 34.34-33.78.

TFBM: ^1H NMR (600 MHz, $CDCl_3$, δ/ppm): 3.42 (t, 2H), 3.34 (s, 3H), 2.22-2.14 (m, 2H), 1.84-1.80 (m, 2H). ^{19}F NMR (564 MHz, $CDCl_3$, δ/ppm): −66.47 (t, 3 F). ^{13}C NMR (150 MHz, $CDCl_3$, δ/ppm): 129.99-124.51, 70.57, 58.19, 30.82-30.25, 22.22-22.17.

Electrolyte preparation

Before preparing the electrolyte, all solvents were thoroughly dried by sequential treatment with anhydrous Na_2SO_4, Na-metal, and molecular sieves (4 Å) prior to use. The electrolyte mentioned in this manuscript was prepared by dissolving 2.0 mmol (for NMR, 1.0 mmol) LiFSI in 1.0 mL solvent of PM, BM, TFPM, or TFBM in an Ar filled glovebox (25 °C, $O_2 < 0.01$ ppm, $H_2O < 0.01$ ppm). For TFEM, 0.1 mmol LiFSI and 1.0 mL solvent were mixed together, but LiFSI cannot be completely dissolved, thus the supernatant was taken for analysis.

Electrode preparation

The NMC powder, acetylene black (Li400, Denka Black), and poly (vinylidene fluoride) (PVDF, HSV900, Kynar) were mixed in N-methyl-2-pyrrolidone (NMP, 99.9%) using a Thinky (AR-100) mixer at a weight ratio of 80: 12: 8 for 10 h. Then the slurry was evenly coated on an Al foil and dried under vacuum at 120 °C for 10 h. The active mass loading of NMC positive electrode was controlled at ~3.5 mg cm^{-2} or ~19 mg cm^{-2} for high-loading test.

Materials characterization

Nuclear magnetic resonance (NMR) measurements were performed on an AVANCE NEO 600 MHz instrument (Bruker). The Raman spectrum of the electrolyte was tested using a QE Pro spectrometer (Ocean Optics) with an emission wavelength of 532 nm. Differential scanning calorimetry (DSC) measurement was performanced in the temperatures range from 30 to −150 °C at a scanning speed of 5 °C min^{-1} with a DSC 214 polyma (NETZSCH). The density and viscosity of electrolyte were measured by a SVM3001 viscometer (Anton Paar) with the temperatures range from 30 to −40 °C. Deposition morphology of Li was observed using a MAIA3 scanning electron microscopy (SEM, TESCAN Brno, s.r.o.). The chemical components on the Li-metal negative electrode surface were analyzed by XPS (PerkinElmer PHI 1600 ESCA). The cell was disassembled in the Ar filled glovebox, of which the electrode was rinsed with the corresponding electrolyte solvent three times and dried under vacuum. The washed electrode was transferred from the glovebox to the XPS chamber directly without exposure to air for the XPS test. The Ar^+ sputtering for the XPS depth-profiling was carried out at a beam energy of 500 eV.

Electrochemical measurement

All the coin-cells were assembled in a standard 2032-configuration in the Ar filled glovebox. Linear sweep voltammetry (LSV), chronoamperometry (CA), electrochemical floating test, and electrochemical impedance spectroscopy (EIS) were carried out using a Potentiostat (VMP3, Bio-Logic). The ionic conductivity was measured by EIS method using a Pt||electrolyte||Pt parallel cell with the temperatures range from 40 to −40 °C. The EIS spectrum was collected within a frequency range of 1 MHz to 10 mHz with a voltage amplitude of 10 mV. The measurements were recorded with 6 data points per decade of frequency to ensure sufficient resolution. CA test was conducted by holding Li||Al cell (40 µL electrolyte) at 4.5 V for 24 h. LSV was tested in a three-electrode system with Al as the working electrode, Li as both the counter and reference electrodes from open circuit voltage (OCV) to 7.0 V at a scanning rate of 1.0 mV s^{-1}. Tafel curve was obtained from LSV at a scan rate of 0.5 mV s^{-1} on a Li||Li symmetric cell (40 µL electrolyte). The value of the exchange current density was calculated by the Tafel equation:

$$\eta = a + b\log i \qquad (1)$$

The cycling tests of Li||Cu and Li||NMC coin cells, and Li||NMC pouch cells were performed using a LAND CT2001A instrument (Wuhan Jinnuo Electronic Co. Ltd.) at different temperatures. The Li|| NMC coin cells were cycled at different rates within the voltage range of 2.8–4.4 V. Three formation cycles at 0.1 C were performed for all coin cells at 30 °C before long-term cycling. The NMC positive electrode was cut into circular pieces with a diameter of 12 mm, and each coin cell used 80 µL electrolyte. The pouch cells were cycled in the voltage range of 2.8–4.4 V at 500 mA for the initial three formation cycles, and then at 1200 mA (25 °C) or 310 mA (−40 °C) for the subsequent cycles. The cycling of the pouch cells was tested under a fixing device to provide 100 kPa external pressure. For the coin cell with a 3.5 mg cm^{-2} NMC811-positive electrode, the current density is 0.74 mA cm^{-2} at 1 C. For the coin cell with a 19 mg cm^{-2} NMC811-positive electrode, the current density is 4.0 mA cm^{-2} at 1 C. For the coin cell with a 3.5 mg cm^{-2} NMC9055-positive electrode, the current density is 0.75 mA cm^{-2} at 1 C.

For Li||Cu cells, 500 µm thick Li foil with diameter of 8 mm, one layer of 19 mm Celgard 2500 separator, 14 mm diameter Cu foil, and 40 µL electrolyte were used. For cycling test, after three activation cycles (plating 1 h with a current density of 0.05 mA cm^{-2} and then stripping to 1.0 V), 1.0 mAh cm^{-2} of Li was plated on the Cu electrode, followed by stripping to 1.0 V. For the Aurbach method[43] tested at 30 °C and −40 °C, with a current density of 1.0 mA cm^{-2}, 5.0 mAh cm^{-2} of Li was firstly plated on the Cu electrode and stripped fully. Then a Li reservoir of 5.0 mAh cm^{-2} was plated on Cu electrode, followed by 10 cycles of Li plating and stripping with a current density of 1.0 mA cm^{-2} and a capacity of 1.0 mAh cm^{-2}. Lastly, all deposition Li was stripped completely to 1.0 V. When tested at −60 °C, the current density and corresponding capacity decreased to 0.1 mA cm^{-2} and 0.1 mAh cm^{-2}, respectively.

The cell for the electrochemical quartz crystal microbalance (EQCM) test consists of a gold-coated quartz crystal (9 MHz AT-cut quartz, 5 mm diameter Au)[45,46], as the working electrode, a Li metal as the counter electrode, and 3.0 mL electrolyte in the Ar-filled glovebox. The mass change of working electrode can be calculated from the collected frequency of quartz crystal by QCM922 quartz crystal microbalance with following equation:

$$\triangle f = -\frac{2f_0^2}{A\sqrt{\rho_Q \mu_Q}}\triangle m \qquad (2)$$

where $\triangle f$ is the frequency change of the gold-coated quartz crystal electrode, f_0^2 is the resonant frequency of the quartz crystal, A is the active crystal surface, ρ_Q is the density of quartz (2.648 g cm^{-3}) μ_Q is the shear modulus of quartz (2.947×10^{11} g cm^{-1} s^{-2}), and $\triangle m$ is the mass change of the electrochemical process in working electrode. The process was performed at a constant current of 0.1 mA cm^{-2} for 300 s by VersaSTAT 3 Potentiostat/Galvanostat, followed by stood still for 400 s and concurrently maintained the frequency measurement to obtain the dissolution mass.

Theoretical calculations

Density functional theory (DFT) calculations were performed using the Gaussian 16 package. The molecular geometries of the ground states were optimized, and the frequency analysis was carried out to ensure the optimized stationary point at the B3LYP/6-311 + G (d, p) level. The restrained electrostatic potentials (RESP) were calculated by Multiwfn 3.8 programs[28]. The binding energy between Li^+ ions and solvent molecules solvent was calculated as: $E_b = E_{total} - (E_{Li}^+ + E_{solvent})$, where E_{total} is the total energy of the Li^+–solvent complexes, E_{Li}^+ and $E_{solvent}$ are the energy of the individual Li^+ ion and solvent molecule, respectively.

Molecular dynamics (MD) simulations were performed by employing the GROMACS 2018 program[52]. The optimized potentials for a liquid simulations all-atom (OPLS-AA) force field were adopted to described molecules and ions. 30 LiFSI and 145 PM molecules, or 30 LiFSI and 125 BM molecules, or 30 LiFSI and 129 TFPM molecules, or 30 LiFSI and 110 TFBM molecules were put into the simulation box according to the molar ratio in electrolytes, respectively. Firstly, the steepest descent method was employed to minimize the initial energy generated for each system. Then 8 ns simulation was carried out in the canonical ensemble (NVT) under Nosé-Hoover thermostat. Another 40 ns simulation was performed in the isothermal-isobaric ensemble (NPT) by Parrinello-Rahman barostat. Finally, the final 30 ns simulation for analysis to obtain coordination numbers and radial distribution functions (RDF).

Data availability

All data supporting the findings of this study are included in the Article and its Supplementary Information. Source data are provided with this paper.

References

1. Zhang, X., Yang, Y. & Zhou, Z. Towards practical lithium-metal anodes. *Chem. Soc. Rev.* **49**, 3040 (2020).
2. Liu, J. et al. Pathways for practical high-energy long-cycling lithium metal batteries. *Nat. Energy* **4**, 180 (2019).
3. Hwang, J.-Y., Park, S.-J., Yoon, C. S. & Sun, Y.-K. Customizing a Li-metal battery that survives practical operating conditions for electric vehicle applications. *Energy Environ. Sci.* **12**, 2174 (2019).
4. Xu, W. et al. Lithium metal anodes for rechargeable batteries. *Energy Environ. Sci.* **7**, 513 (2014).
5. Jagger, B. & Pasta, M. Solid electrolyte interphases in lithium metal batteries. *Joule* **7**, 2228 (2023).
6. Zhang, S. S., Xu, K. & Jow, T. R. The low temperature performance of Li-ion batteries. *J. Power Sources* **115**, 137 (2003).
7. Holoubek, J. et al. Tailoring electrolyte solvation for Li metal batteries cycled at ultra-low temperature. *Nat. Energy* **6**, 303 (2021).

8. Kang, X. Electrolytes and interphases in Li-ion batteries and beyond. *Chem. Rev.* **114**, 11503 (2014).
9. Xu, Q. et al. Li_2ZrF_6-based electrolytes for durable lithium metal batteries. *Nature* **637**, 339 (2025).
10. Zhang, W. et al. Multifunctional electrolyte additive for high power lithium metal batteries at ultra-low temperatures. *Nat. Commun.* **16**, 3344 (2025).
11. Tian, C., Qin, K. & Suo, L. Concentrated electrolytes for rechargeable lithium metal batteries. *Mater. Futures* **2**, 012101 (2023).
12. Yamada, Y., Wang, J., Ko, S., Watanabe, E. & Yamada, A. Advances and issues in developing salt-concentrated battery electrolytes. *Nat. Energy* **4**, 269 (2019).
13. Yamada, Y., Yaegashi, M., Abe, T. & Yamada, A. A superconcentrated ether electrolyte for fast-charging Li-ion batteries. *Chem. Commun.* **49**, 11194 (2013).
14. Suo, L., Hu, Y. S., Li, H., Armand, M. & Chen, L. A new class of Solvent-in-Salt electrolyte for high-energy rechargeable metallic lithium batteries. *Nat. Commun.* **4**, 1481 (2013).
15. Chen, Y. et al. Steric effect tuned ion solvation enabling stable cycling of high-voltage lithium metal battery. *J. Am. Chem. Soc.* **143**, 18703 (2021).
16. Jie, Y. et al. Towards long-life 500 Wh kg^{-1} lithium metal pouch cells via compact ion-pair aggregate electrolytes. *Nat. Energy* **9**, 987 (2024).
17. Zhang, G. et al. Molecular design of competitive solvation electrolytes for practical high-energy and long-cycling lithium-metal batteries. *Adv. Funct. Mater.* **34**, 2312413 (2023).
18. Cui, Z. et al. Molecular anchoring of free solvents for high-voltage and high-safety lithium metal batteries. *Nat. Commun.* **15**, 2033 (2024).
19. Park, E. et al. Exploiting the steric effect and low dielectric constant of 1,2-dimethoxypropane for 4.3 V lithium metal batteries. *ACS Energy Lett.* **8**, 179 (2022).
20. Yu, Z. et al. Rational solvent molecule tuning for high-performance lithium metal battery electrolytes. *Nat. Energy* **7**, 94 (2022).
21. Zhao, Y. et al. Fluorinated ether electrolyte with controlled solvation structure for high voltage lithium metal batteries. *Nat. Commun.* **13**, 2575 (2022).
22. Ding, K. et al. Tuning the solvent alkyl chain to tailor electrolyte solvation for stable Li-metal batteries. *ACS Appl. Mater. Interfaces* **14**, 44470 (2022).
23. Li, A. M. et al. Methylation enables the use of fluorine-free ether electrolytes in high-voltage lithium metal batteries. *Nat. Chem.* **16**, 922 (2024).
24. Wu, L. Q. et al. Unveiling the role of fluorination in hexacyclic coordinated ether electrolytes for high-voltage lithium metal batteries. *J. Am. Chem. Soc.* **146**, 5964 (2024).
25. Wei, Y. et al. Moderate solvation structures of lithium ions for high-voltage lithium metal batteries at −40 °C. *Energy Environ. Sci.* **18**, 786 (2025).
26. Lu, T. & Chen, F. Multiwfn: a multifunctional wavefunction analyzer. *J. Comput. Chem.* **33**, 580 (2012).
27. Lu, T. A comprehensive electron wavefunction analysis toolbox for chemists, Multiwfn. *J. Chem. Phys.* **161**, 082503 (2024).
28. Tian, L. U. & Fei-Wu, C. Comparison of computational methods for atomic charges. *Acta Phys.-Chim. Sin.* **28**, 1 (2012).
29. Lu, T. & Chen, F. Quantitative analysis of molecular surface based on improved Marching Tetrahedra algorithm. *J. Mol. Graph. Model.* **38**, 314 (2012).
30. Li, Z. et al. Non-polar ether-based electrolyte solutions for stable high-voltage non-aqueous lithium metal batteries. *Nat. Commun.* **14**, 868 (2023).
31. Shi, J. et al. An amphiphilic molecule-regulated core-shell-solvation electrolyte for Li-metal batteries at ultra-low temperature. *Angew. Chem. Int. Ed.* **62**, e202218151 (2023).
32. Choi, I. R. et al. Asymmetric ether solvents for high-rate lithium metal batteries. *Nat. Energy* **10**, 365 (2025).
33. Qiao, R. et al. Non-fluorinated electrolytes with micelle-like solvation for ultra-high energy density lithium metal batteries. *Chem* **11**, 102306 (2024).
34. Kang, C. et al. Low-solvent-coordination solvation structure for lithium-metal batteries via electric dipole-dipole interaction. *Angew. Chem. Int. Ed.* **63**, e202412703 (2024).
35. Cheng, F. et al. Modulating interfacial solvation via ion dipole interactions for low-temperature and high-voltage lithium batteries. *Angew. Chem. Int. Ed.* **64**, e202415853 (2024).
36. Xia, Y. et al. Designing an asymmetric ether-like lithium salt to enable fast-cycling high-energy lithium metal batteries. *Nat. Energy* **8**, 934 (2023).
37. Zhou, P. et al. Rational lithium salt molecule tuning for fast charging/discharging lithium metal battery. *Angew. Chem. Int. Ed.* **63**, e202316717 (2024).
38. Zhang, G. et al. Amonofluoride ether-based electrolyte solution for fast-charging and lowtemperature non-aqueous lithium metal batteries. *Nat. Commun.* **14**, 1081 (2023).
39. Zhang, J. et al. Weakly solvating cyclic ether electrolyte for high-voltage lithium metal batteries. *ACS Energy Lett.* **8**, 1752 (2023).
40. Piao, N. et al. Designing temperature-insensitive solvated electrolytes for low-temperature lithium metal batteries. *J. Am. Chem. Soc.* **146**, 18281 (2024).
41. Zhao, Z. et al. Leveraging ion pairing and transport in localized high-concentration electrolytes for reversible lithium metal anodes at low temperatures. *Angew. Chem. Int. Ed.* **63**, e202412239 (2024).
42. Yao, Y. X. et al. Regulating interfacial chemistry in lithium-ion batteries by a weakly solvating electrolyte. *Angew. Chem. Int. Ed.* **60**, 4090 (2021).
43. Adams, B. D., Zheng, J., Ren, X., Xu, W. & Zhang, J. G. Accurate determination of coulombic efficiency for lithium metal anodes and lithium metal batteries. *Adv. Energy Mater.* **8**, 1702097 (2018).
44. Ji, Y. et al. In situ probing the origin of interfacial instability of Na metal anode. *Chem* **9**, 2943 (2023).
45. Tułodziecki, M., Tarascon, J. M., Taberna, P. L. & Guéry, C. Catalytic reduction of TFSI-containing ionic liquid in the presence of lithium cations. *Electrochem. Commun.* **77**, 128 (2017).
46. Liu, T. et al. In situ quantification of interphasial chemistry in Li-ion battery. *Nat. Nanotechnol.* **14**, 50 (2019).
47. Li, Z. et al. A tetrahydropyran-based weakly solvating electrolyte for low-temperature and high-voltage lithium metal batteries. *Adv. Energy Mater.* **15**, 2404120 (2024).
48. Yin, X. et al. Solvent-derived organic-rich SEI enables capacity enhancement for low-temperature lithium metal batteries. *Joule* **9**, 101823 (2025).
49. Cui, Z. et al. Push-pull electrolyte design strategy enables high-voltage low temperature lithium metal batteries. *J. Am. Chem. Soc.* **146**, 27644 (2024).
50. Zhang, W. et al. A reversible self-assembled molecular layer for lithium metal batteries with high energy/power densities at ultra-low temperatures. *Energy Environ. Sci.* **17**, 4531 (2024).
51. Guo, X. et al. Breaking aggregation state to achieve low-temperature fast charging of lithium metal batteries. *Angew. Chem. Int. Ed.* **64**, e202414613 (2025).
52. Abraham, M. J. et al. GROMACS: High performance molecular simulations through multi-level parallelism from laptops to supercomputers. *SoftwareX* **1-2**, 19 (2015).

Acknowledgements

This work was supported by the National Natural Science Foundation of China (Nos. 92372123, 22209050), and Natural Science Foundation of Guangdong Province (Nos. 2022B1515020005, 2023B1515130004).

Author contributions

Q.Z. conceived the idea and directed the project. K.D. and Z.P. proposed the concept and designed the experiments. Z.P. and M.L. conducted the electrochemical experiments and analysis. R.Q. and C.X. performed the theoretical calculations. Z.P. and J.S. conducted the solvent synthesis and NMR analysis. Y.X. performed the XPS measurements. X.G. helped with the pouch cell assembly and evaluation. F.W. and K.D. helped with data analysis and mechanism identification. Z.P. wrote the draft paper, Q.Z. and Y.C. edited and polished the paper. All authors contributed to the interpretation of the results.

Competing interests

The authors declare no competing interests.

Additional information

Supplementary information The online version contains supplementary material available at https://doi.org/10.1038/s41467-025-67290-7.

Correspondence and requests for materials should be addressed to Qifeng Zheng.

Peer review information *Nature Communications* thanks Zheng Chen (eRef) who co-reviewed with Hongpeng Gao (ECR)and the other anonymous reviewer(s) for their contribution to the peer review of this work. A peer review file is available.

Reprints and permissions information is available at http://www.nature.com/reprints

Publisher's note Springer Nature remains neutral with regard to jurisdictional claims in published maps and institutional affiliations.

Open Access This article is licensed under a Creative Commons Attribution-NonCommercial-NoDerivatives 4.0 International License, which permits any non-commercial use, sharing, distribution and reproduction in any medium or format, as long as you give appropriate credit to the original author(s) and the source, provide a link to the Creative Commons licence, and indicate if you modified the licensed material. You do not have permission under this licence to share adapted material derived from this article or parts of it. The images or other third party material in this article are included in the article's Creative Commons licence, unless indicated otherwise in a credit line to the material. If material is not included in the article's Creative Commons licence and your intended use is not permitted by statutory regulation or exceeds the permitted use, you will need to obtain permission directly from the copyright holder. To view a copy of this licence, visit http://creativecommons.org/licenses/by-nc-nd/4.0/.

© The Author(s) 2025